

Model Based, Direct Flux Vector Control of Permanent Magnet Synchronous Motor Drives

Original

Model Based, Direct Flux Vector Control of Permanent Magnet Synchronous Motor Drives / Boazzo, Barbara; Pellegrino, GIAN - MARIO LUIGI. - In: IEEE TRANSACTIONS ON INDUSTRY APPLICATIONS. - ISSN 0093-9994. - STAMPA. - 51:4(2015), pp. 3126-3136. [10.1109/TIA.2015.2399619]

Availability:

This version is available at: 11583/2589155 since: 2015-12-04T16:28:07Z

Publisher:

IEEE

Published

DOI:10.1109/TIA.2015.2399619

Terms of use:

This article is made available under terms and conditions as specified in the corresponding bibliographic description in the repository

Publisher copyright

(Article begins on next page)

Model-Based, Direct Flux Vector Control of Permanent Magnet Synchronous Motor Drives

Barbara Boazzo and Gianmario Pellegrino

Department of Energy, Politecnico di Torino, Turin, Italy

Abstract— This paper proposes a direct flux vector control strategy with no need for regulators tuning, suitable for Permanent Magnet (PM) Synchronous Machine drives. The controller operates in stator flux coordinates, and calculates the inverter reference voltages in a model-based fashion, taking advantage of a novel equation for the explicit evaluation of the torque angle error. The inverter current and voltage limits are exploited in a parameter-independent way. The method segregates the machine parameters into a single block, so to make it very easy to switch from one machine to another. Experimental results are reported for a PM-assisted synchronous reluctance motor drive example, characterized by significant saturation and cross-saturation. State of the art control techniques such as current vector control and non-model-based direct flux vector control are also considered, for the sake of comparison, in simulations and experiments.

I. INTRODUCTION

Direct torque and flux control, commercially known as DTC, is widely adopted for AC motor drives thanks to its fast dynamic characteristics and robust implementation. The direct control of the flux linkage vector amplitude and phase facilitates the exploitation of the inverter voltage and current limits in the flux weakening speed region [1, 2, 22]. The ease of implementation of DTC and the insensitiveness to the parameters of the controlled machine are precious for flux-weakening operation and related applications.

The Direct Flux Vector Control (DFVC) combines the features of the DTC with the ones of current vector controller: constant switching frequency and straightforward limitation of the current amplitude [3]. The closed-loop controlled variables are the amplitude of the stator flux linkage and the current component in quadrature with the flux vector. These two are combined to obtain direct flux and torque control. So far, two proportional-integral (PI) regulators were used in for the two control loops. A third PI regulator handles the maximum torque per voltage (MTPV) limit [3]. This paper presents a model-based version of the DFVC where the PI regulators are replaced by closed form equations producing the inverter voltage reference values from the torque and flux linkage amplitude set points and feedbacks. The proposed approach has three main advantages: 1) no need for PI calibration; 2) the MTPV limit handled via a simple saturation block; 3) the dynamic response of closed loop control is invariant with the torque and speed operating point (whereas PI regulators would require gain adaptation throughout the torque – speed domain [18]).

A review of the principles of predictive controllers and DFVC is first reported. Then the novel algorithm is introduced, and its key-blocks described mathematically and commented. The key enabling technology for the proposed

control algorithm is the predictive current and flux linkage observer. It is known that the delay of actuation of the digital controller can produce chattery responses, in model-based control. Hence, the observer performs one-step-ahead extrapolation of the system states and controlled variables to compensate for such delay [4]. The tests presented in the paper refer to a PM-assisted Synchronous Reluctance (PMASR) motor drive, purposely chosen for its extremely nonlinear magnetic behavior. Within the class of PM synchronous machines, this machine can be considered as the most challenging example nonlinear magnetic model. Therefore, the predictive flux and current observer incorporates real-time re-evaluation of the dq apparent inductances at every sampling time. Yet, machines with simpler magnetic models can be controlled with this algorithm, as a subcase of the presented machine example. Simulation and experimental results are reported, including performance comparison with two state of the art control techniques: Current Vector Control (CVC) [5] and PI-based DFVC [3].

The original contributions of the paper are: 1) the load angle error is expressed explicitly, via a closed-form equation; 2) the control algorithm has the machine parameters segregated in a single block in non-manipulated form, for the sake of minimum tuning and commissioning effort; 3) torque reversal of highly salient machines is firstly analyzed. Depending on the machine type, torque reversal can become critical when the flux vector is directly controlled.

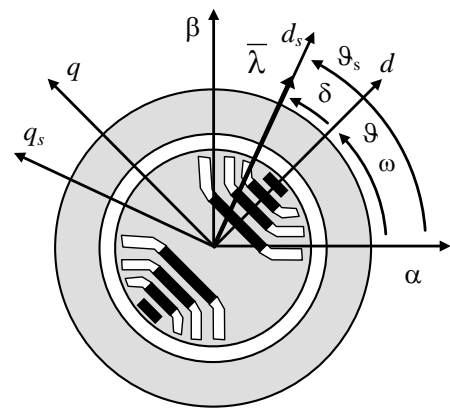


Figure 1. Definition of the reference frames and the phase angles: stationary frame $\alpha\beta$, rotor synchronous frame dq , stator flux synchronous frame $d_s q_s$; load angle δ , rotor position θ , flux linkage frame position θ_s .

II. BASICS OF THE PROPOSED CONTROL

The stator flux coordinates $d_s q_s$ are defined in Fig. 1. The d_s voltage component regulates the amplitude of the flux linkage vector λ , while the q_s voltage component controls the quadrature current i_{q_s} , with the load torque angle δ acting as

an intermediate variable. The angular quantities introduced in Fig. 1 are the load angle δ , the stator flux coordinate θ_s , the rotor position θ and angular frequency ω . The rotor reference dq is also used throughout the paper, when dealing with the magnetic model of the machine.

A. Digital Implementation and Predictive Observer

The model-based control algorithm takes advantage of the inverse model of the electrical machine, to relate the control errors to the output voltage commands via explicit equations. The technical challenges associated with the design of such control are the **nonlinear magnetic model**, common to all saturated or salient PM machines, and the one-step **delay of actuation** introduced by the digital controller.

This implementation is based on Space Vector Modulation at constant switching frequency, and the sampling period coincides with the switching period of the modulation. Fig. 2 provides graphical representation of the sequence of events during consecutive sample instants and serves as an introduction of the notations adopted in the rest of the document. The real-time digital controller samples the measured quantities at fixed time instants, t_k being the present one. The notation $(k-1)$ indicates the past value $t_{k-1} = t_k - T_s$. The voltage command reference $v^*(k)$ is evaluated after the sampling at t_k and executed at time $t_{k+1} = t_k + T_s$. The reference at (k) turns into the actual voltage at $(k+1)$: $v^*(k) = v(k+1)$ and is active between t_{k+1} and t_{k+2} .

Variables with a “hat” in Fig. 2 are observed quantities. When the hat is associated to $(k+1)$ it means that the observed quantity is also predicted at execution time $(k+1)$. The literature [4,6-7] points out that the extrapolation of the machine states at one step ahead is useful for the correct evaluation of the reference voltages, and to avoid chattery response [8,9]. Thus, the digital controller processes data available at sampling time t_k to extrapolate the machine states at execution time t_{k+1} . This task is fulfilled by the “Predictive Observer” block, described later in the paper.

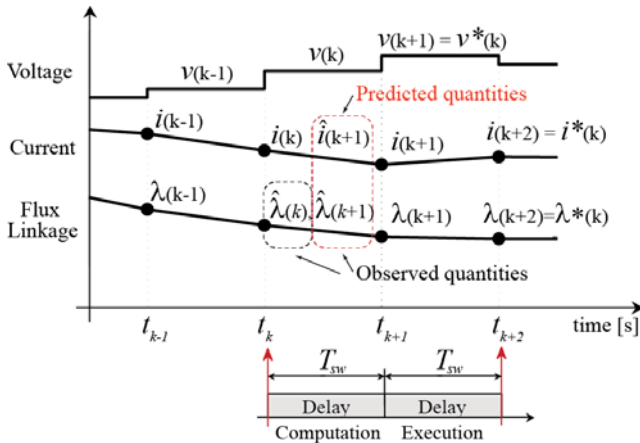


Figure 2. Delay related to digital implementation. The voltage reference calculated at time (k) is actuated at time $(k+1)$. The predictive observer outputs the current and flux-linkage predictions at time $(k+1)$. The setpoints of time (k) are reached at time $(k+2)$.

Going back to Fig. 2, it must be noticed that the flux linkage and current references (“star” superscript) are reached after **two sampling periods**: e.g. $\lambda^*(k) = \lambda(k+2)$. One-step delay accounts for time from sampling to execution (k to $k+1$) and the second is the one needed to complete the execution of the voltage command (commands are latched from $k+1$ to $k+2$). This to say that dead-beat control has an execution delay of **two beats**. For large step variations of the torque and flux linkage reference the time to target grows further, due to the finite Volt-seconds supplied by the power converter in one sampling period. Model errors deteriorate the response and further prolong the time to target, because the calculated voltage vector is deviated and the control response becomes chattery.

B. Direct Flux Vector Control Scheme

The block diagram of the proposed control algorithm is reported in Fig. 3. From left to right from, the reference torque signal T^* is first found. The flux linkage reference is determined from T^* according to the Maximum Torque per Ampere (MTPA) strategy. The flux reference is therefore saturated to comply with the inverter voltage limit. Below the corner speed such saturation is ineffective. The saturated flux linkage reference λ^* is used to produce the quadrature current reference i_{qs}^* , via the inverse of the torque equation (1), given the number of pole pairs p :

$$T = \frac{3}{2} \cdot p \cdot \lambda \cdot i_{qs} \quad (1)$$

The second reference quantity i_{qs}^* is also saturated, to account for the converter current limit I_{max} . After the respective saturations, the control errors are calculated and then manipulated with closed-form equations to obtain the reference voltage vector and then the inverter commands.

C. Maximum Current and Voltage Limitations

Let I_{max} be the maximum inverter current, the limit applied to i_{qs} is:

$$i_{qs,max} = \sqrt{I_{max}^2 - i_{ds}^2} \quad (2)$$

The magnitude of the flux linkage vector is saturated according to the electrical operating speed ω and the available voltage V_{max} . In formulas:

$$\lambda_{max} = \frac{|V_{max} - R_s i_{qs}^* \text{sign}(\omega)|}{|\omega|} \quad (3)$$

V_{max} is proportional to the dc-link voltage V_{dc} , by way of a scale factor depending on the choice of exploiting or not the over-modulation region of the converter. R_s is the stator resistance. Its contribution can be neglected in (3) in some cases, depending on the motor power rating.

D. Maximum Torque per Voltage Limit

In [3] and [12] the Maximum Torque per Voltage (MTPV) limited region is exploited by limitation of the load angle to an appropriate maximum value. The task would normally require one additional PI-regulator. Instead, this new implementation has the torque angle error $\Delta\delta$ in explicit form in the q_s control loop (Fig. 3 in the red box). Direct saturation of the load angle error is possible, in place of the dedicated PI regulator.

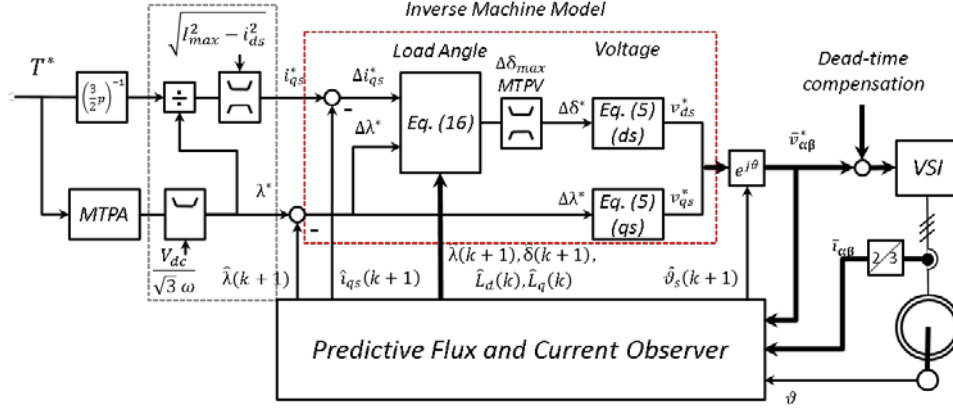


Figure 3. Block diagram of the predictive Direct Flux Vector Control. The dotted grey block contains the maximum current and voltage limitation blocks; the dotted red block contains the closed-form construction of the reference voltage vector. VSI stands for “Voltage Supplied Inverter”.

III. MODEL-BASED CONTROL BLOCKS

This section introduces the blocks in the “Inverse Machine Model” red rectangle of Fig. 3. The blocks are described from right to left.

A. Voltage Equation

The voltage equations reported to the flux-linkage reference frame d_s, q_s are:

$$\begin{cases} v_{ds} = R_s \cdot i_{ds} + \frac{d\lambda}{dt} \\ v_{qs} = R_s \cdot i_{qs} + \left(\frac{d\delta}{dt} + \omega \right) \cdot \lambda \end{cases} \quad (4)$$

In discrete-time form, with sampling period T_s , the equations become:

$$\begin{cases} v_{ds}^*(k) = R_s \cdot \hat{i}_{ds}(k+1) + \frac{\Delta\lambda^*}{T_s} \\ v_{qs}^*(k) = R_s \cdot \hat{i}_{qs}(k+1) + \left[\frac{\Delta\delta^*}{T_s} + \omega(k) \right] \cdot \hat{\lambda}(k+1) \end{cases} \quad (5)$$

Where the control errors $\Delta\lambda^*$ and $\Delta\delta^*$ are:

$$\Delta\lambda^* = \lambda^*(k) - \hat{\lambda}(k+1) \quad (6a)$$

$$\Delta\delta^* = \delta^*(k) - \hat{\delta}(k+1) \quad (6b)$$

The discrete form equation (5) was obtained with forward Euler discretization, with reference to the sampling period going from $(k+1)$ to $(k+2)$. This in consideration of the definitions given in II.A: time (k) reference voltages are equal to actual voltage from time $(k+1)$ to $(k+2)$. Therefore, flux vector set points $\lambda^*(k), \delta^*(k)$ will be reached at time $(k+2)$, after the execution of $v^*(k)$ is completed. The assumption under (5) and (6) is $\lambda(k+2) = \lambda^*(k)$ and $\delta(k+2) = \delta^*(k)$.

The voltage model (5) outputs the voltage components v_{ds}, v_{qs} according to the target increments of the flux amplitude and of the load angle, respectively. The load angle variation $\Delta\delta^*$ comes from block “Eq. (16)” in Fig. 3, according to the two control errors $\Delta\lambda$ and Δi_{qs} . This equation is formalized in the following subsections, as a result of magnetic model manipulation. The saturation block MTPV is commented later, in subsection III.D.

B. Magnetic Model

The magnetic model of the PM synchronous machine is experimentally identified and stored in the form of dq flux

linkage look-up tables. Experimental flux linkage curves are reported in Fig. 5, for the machine under test. The look-up tables are used in the flux observer, as shown later, in subsection IV.A. However, when coming to on-line model manipulation, it is convenient to introduce an approximated model based on dq inductances:

$$\begin{cases} \lambda_d = L_d(i_d, i_q) \cdot i_d + \lambda_m \\ \lambda_q = L_q(i_d, i_q) \cdot i_q \end{cases} \quad (7)$$

The PM flux linkage is represented by the single parameter λ_m , while inductances L_d and L_q vary with i_d and i_q due to saturation and cross-saturation effects. Cross-saturation has no dedicated terms L_{dq}, L_{qd} in (7), but its effects are implicitly taken into account in the form of L_d variations with i_q and L_q variations with i_d [10]. As an example, Fig. 5b shows the apparent dq inductances of the motor under test here, corresponding to the experimental flux linkage curves of Fig. 5a. The ratings of the machine are reported in Table I. In the following the dependency of L_d, L_q from the i_d, i_q operating condition will be taken into account even if not explicitly expressed for the sake of a shorthand notation. The effect of λ_m detuning due to temperature variation is commented later in the paper.

C. Load Angle Equation

Torque expression in dq coordinates (8) is:

$$T = \frac{3}{2}p \cdot (\lambda_d i_q - \lambda_q i_d) \quad (8)$$

To put in evidence the state variables λ and δ , the i_d, i_q components are first expressed in terms of $\lambda_d, \lambda_q, \lambda_m$ by inversion of (7). Hence, the dq flux components of (8) are turned into polar coordinates: $\lambda_d = \lambda \cos(\delta), \lambda_q = \lambda \sin(\delta)$ to obtain expression (9).

$$T = \frac{3}{2}p \cdot \left(\frac{\lambda \lambda_m}{L_d} \sin(\delta) - \frac{\lambda^2}{2L_q} (\xi - 1) \sin(2\delta) \right) \quad (9)$$

Where $\xi = L_q/L_d$ is the saliency ratio. The two terms in the parentheses account for permanent magnet and reluctance torque contributions. As usual for DTC, torque can be regulated via the amplitude and phase angle of the

flux linkage vector. This section presents the mathematical derivation of how the load angle δ is related to i_{qs} and λ .

The dq magnetic model (7) is expressed in the stator field oriented frame $d_s q_s$ by a rotation by δ :

$$\begin{cases} \lambda = L_{ds} \cdot i_{ds} + L_{dqs} \cdot i_{qs} + \lambda_m \cos(\delta) \\ 0 = L_{dqs} \cdot i_{ds} + L_{qs} \cdot i_{qs} - \lambda_m \sin(\delta) \end{cases} \quad (10)$$

The inductance terms L_{ds} , L_{dqs} and L_{qs} in the new reference frame depend on L_d , L_q and δ :

$$\begin{bmatrix} L_{ds} & L_{dqs} \\ L_{dqs} & L_{qs} \end{bmatrix} = \begin{bmatrix} L_0 - \Delta L \cos(2\delta) & \Delta L \sin(2\delta) \\ \Delta L \sin(2\delta) & L_0 + \Delta L \cos(2\delta) \end{bmatrix} \quad (11)$$

$$L_0 = \frac{L_d + L_q}{2} \quad \Delta L = \frac{L_q - L_d}{2} \quad (12)$$

The magnetic equations (10) and (11) are manipulated to find a relationship between the control errors $\Delta\lambda$ and Δi_{qs} and the load angle variation $\Delta\delta$. The d_s and q_s components of (10) are time differentiated leading to equations (13a) and (14a), respectively. The former refers to the d_s component of (10), the latter to the q_s component.

$$\frac{di_{ds}}{dt} = A \cdot \frac{d\lambda}{dt} + B \cdot \frac{di_{qs}}{dt} + C \cdot \frac{d\delta}{dt} \quad (13a)$$

$$\begin{cases} A = \frac{1}{L_0 - \Delta L \cos(2\delta)} \\ B = -\frac{\Delta L \sin(2\delta)}{L_0 - \Delta L \cos(2\delta)} \\ C = -\frac{2\Delta L(\sin(2\delta)i_{ds} + \cos(2\delta)i_{qs}) - \lambda_m \sin(\delta)}{L_0 - \Delta L \cos(2\delta)} \end{cases} \quad (13b)$$

$$\frac{di_{qs}}{dt} = B' \cdot \frac{di_{ds}}{dt} + C' \cdot \frac{d\delta}{dt} \quad (14a)$$

$$\begin{cases} B' = -\frac{L_0 + \Delta L \cos(2\delta)}{\Delta L \sin(2\delta)} \\ C' = -\frac{2\Delta L(\cos(2\delta)i_{ds} - \sin(2\delta)i_{qs}) - \lambda_m \cos(\delta)}{\Delta L \sin(2\delta)} \end{cases} \quad (14b)$$

The time derivative of i_{ds} is eliminated by equalizing the right-hand sides of the two equations (13a) and (14a). The variables left after simplification of i_{ds} are λ , i_{qs} and δ :

$$(C - C') \cdot \frac{d\delta}{dt} = (B' - B) \cdot \frac{di_{qs}}{dt} - A \cdot \frac{d\lambda}{dt} \quad (15)$$

After further manipulation the load angle variation in the discrete-time domain is:

$$\Delta\delta^* = \frac{\Delta i_{qs}^* + \frac{[\hat{\xi}(k)-1]}{2L_q(k)} \cdot \Delta\lambda^*}{\frac{\cos[\hat{\delta}(k+1)]}{L_d(k)} \cdot \lambda_m - \frac{[\hat{\xi}(k)-1] \cdot \cos[2\hat{\delta}(k+1)]}{L_q(k)} \cdot \hat{\lambda}(k+1)} \quad (16)$$

Where:

$$\Delta i_{qs}^* = i_{qs}^*(k) - \hat{i}_{qs}(k+1) \quad (17)$$

The load angle variation (16) is a function of the two control errors $\Delta\lambda^*$ and Δi_{qs}^* . Moreover, it is also a function of the magnetic model parameters L_d , L_q , λ_m and of the magnetic states λ and δ , predicted at time $(k+1)$.

Going back to the torque control diagram of Fig. 3, this is now summarized as follows. 1) Torque set point determines the two references i_{qs}^* and λ^* (section II.B). 2) The respective feedback signals $\hat{i}_{qs}(k+1)$ and $\hat{\lambda}(k+1)$ are

calculated by the predictive flux and current observer, and the control errors $\Delta\lambda^*$ (6a) and Δi_{qs}^* (17) follow accordingly; 3) equation (16) is applied, with $\hat{\delta}(k+1)$ and $L_d(k)$, $L_q(k)$ coming from the predictive observer. 4) Finally, the reference voltages $v_{ds}^*(k)$ and $v_{qs}^*(k)$ are calculated using the voltage equations in discrete-time form (5).

According to (16) the load angle variation is coupled to both the direct and quadrature axes $d_s q_s$. It must be noticed that the d_s coupling is related to the reluctance torque and vanishes in non-salient machines ($\xi = 1$). When the saliency ratio is close to one the d_s and q_s control channels are ideally decoupled. However, all saturated synchronous machines tend to have $\xi \neq 1$, also the ones that are isotropic geometric wise, because of saturation. The use of the general expression (16) is convenient, for the sake of control accuracy and general validity of the approach.

D. MTPV Operation

The MTPV limit or pull-out torque limit is encountered at high speed, if the converter current is larger than the machine characteristic current [11]. The MTPV (or maximum torque per flux amplitude) condition is found mathematically by equaling to zero the torque versus load angle partial derivative. Equation (18) is obtained by differentiation of (9):

$$\left. \frac{dT}{d\delta} \right|_{\lambda=const} = \lambda \cdot \left(\frac{\cos(\delta)}{L_d} \cdot \lambda_m - \frac{(\xi-1)\cos(2\delta)}{L_q} \cdot \lambda \right) = 0 \quad (18)$$

If the solution $\lambda = 0$ is excluded, equation (18) becomes:

$$\frac{\cos(\delta)}{L_d} \cdot \lambda_m - \frac{(\xi-1)\cos(2\delta)}{L_q} \cdot \lambda = 0 \quad (19)$$

Equation (19) defines the pullout torque condition as implicit relationship between the load angle δ and the flux amplitude λ , given the machine parameters. Paper [12] shows that the MTPV trajectory (19) is well approximated by a constant load angle δ_{max} in the dq flux linkage plane. The load angle must be limited, in absolute value, to stay under δ_{max} . Such task was implemented in [12] by means of a closed-loop regulator. Instead, the MTPV is handled here by explicit saturation of the load angle to δ_{max} , as represented in the block diagram of Fig. 3.

$$\Delta\delta_{max} = \delta_{max} - \hat{\delta}(k) \quad (20)$$

This is another key simplification of the proposed algorithm with respect to previous schemes. It is worth highlighting that the left-hand side of (19) is also the denominator of the control equation (16), so to say that the MTPV region is a singularity in the domain of the DFVC, as it is also true for DTC. In other words, for $|\delta| > \delta_{max}$ the denominator of (16) becomes negative and the torque controller sees a positive feedback and instability. The limitation of δ to the correct maximum value ensures MTPV exploitation and control stability at the same time. As said, the same considerations are valid also for the more popular DTC.

IV. CURRENT AND FLUX OBSERVER

The flux and current predictive observer presented here operates in consecutive steps:

- 1) the stator flux linkage vector is observed at the present time t_k with a standard scheme.
- 2) inductances $\hat{L}_d(k)$ and $\hat{L}_q(k)$ are derived from observed flux linkages and current measurements;
- 3) the current vector is extrapolated at time $(k+1)$ from current measurements and voltage references at time (k) , in consideration of the just estimated inductances
- 4) The flux linkage vector at time $(k+1)$ is calculated from the t_{k+1} extrapolated currents and the t_k estimated inductances.

The flux observer is schematically described in Fig. 4: Torque estimate at t_{k+1} is also evaluated. The rotor position measured at time (k) is used in the diagram of Fig. 4 for coordinate transformation to the dq rotor frame from the $\alpha\beta$ stator frame, and vice-versa.

A. Observed Flux at Present Time t_k

The flux linkage estimate at t_k comes from the well-known closed loop combination of the voltage and current model of the machine [13]. The voltage model (21), in stator coordinates $\alpha\beta$, is integrated for estimate of the stator flux linkages. The voltage commands at time t_{k-1} are used as voltage signal.

$$\begin{cases} \frac{d\hat{\lambda}_\alpha}{dt} = v_\alpha - R_s i_\alpha + g \cdot (\tilde{\lambda}_\alpha - \hat{\lambda}_\alpha) \\ \frac{d\hat{\lambda}_\beta}{dt} = v_\beta - R_s i_\beta + g \cdot (\tilde{\lambda}_\beta - \hat{\lambda}_\beta) \end{cases} \quad (21)$$

The observer error signal uses the “current model” flux estimates:

$$\begin{cases} \tilde{\lambda}_d = \lambda_d(i_d, i_q) \\ \tilde{\lambda}_q = \lambda_q(i_d, i_q) \end{cases} \quad (22)$$

The observer gain g [rad/s] sets the crossover angular frequency between the low- and high-speed estimation methods. In turn, the voltage model is predominant above g [rad/s] whereas the current model serves the low speed region $\omega < g$ [rad/s]. The current model (22) consists of two look-up tables, with input the dq current measurements at t_k .

The two-dimensional look-up tables are derived from the experimental identification of the machine under test. The flux linkage curves are reported in Fig. 5a. They were obtained with the method described in [14]. Other identification techniques are valid as well [10,15]. Because the current model is critical only in the low speed region ($\omega < g$ [rad/s]), a very accurate identification of the magnetic model is not always compulsory. Simplified magnetic models can be effective for example if low speed operation at full load is not required, or where the starting torque is moderate and also with machines having less pronounced inductance variations inductances with i_d, i_q . Moreover, self-commissioning methods for seamless identification are under way [19].

B. Adaptive Evaluation of L_d and L_q .

The flux linkages observed at time (k) in the stationary frame $\alpha\beta$ are counter-rotated to the dq synchronous frame to obtain $\hat{\lambda}_d(k)$ and $\hat{\lambda}_q(k)$. The dq inductances are derived according to the three-parameter magnetic model (7):

$$\begin{cases} \hat{L}_d(k) = \frac{\hat{\lambda}_d(k) - \lambda_m}{i_d(k)} \\ \hat{L}_q(k) = \frac{\hat{\lambda}_q(k)}{i_q(k)} \end{cases} \quad (23)$$

The inductances (23) contain real-time, full information about the magnetic state of the machine, coming from the time (k) observed flux linkage vector. At low speed such information comes from the LUTs, whereas at high speed it comes from back-emf integration. The next subsections show how $L_d(k)$, $L_q(k)$ are used for extrapolation of the current and flux linkage vectors at time $(k+1)$. Moreover, they are also used in the control equation (16). Figs. 5b and 5c show the values of L_d and L_q across the dq current domain for the motor under test. The contours were derived from the flux linkage curves of Fig. 5a, by application of (23). It is evident that, at least for this machine, the real-time adaptation (23) is mandatory, because the inductances have large variations from one operating point to another. The use of constant or inaccurate values of L_d and L_q would produce wrong forward extrapolation of the control feedbacks (current and flux), and also imprecise evaluation of the voltage vector through (16) and (5). Section V reports comparative results on this issue.

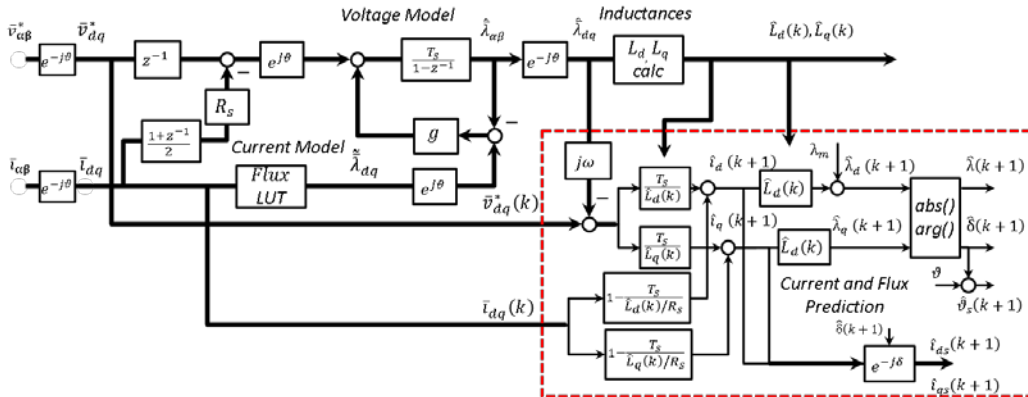


Figure 4. Predictive flux linkage and current observer. The dashed rectangle includes and puts in evidence the predictive part of the observer. Where non specified, the variables are intended at present time (k) .

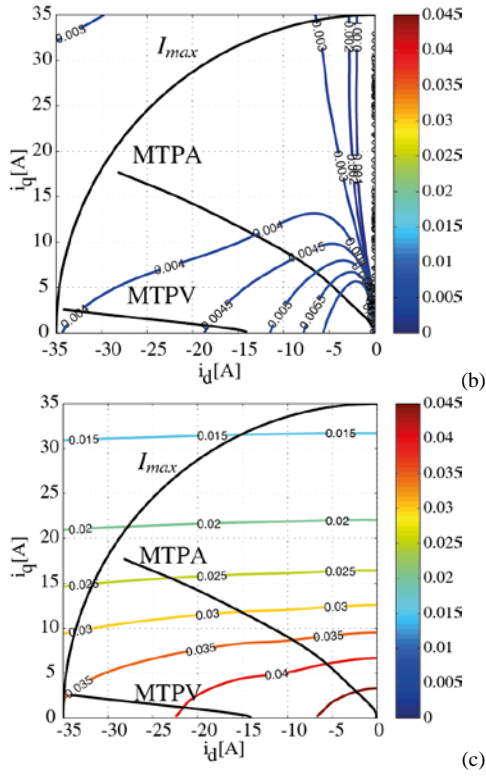
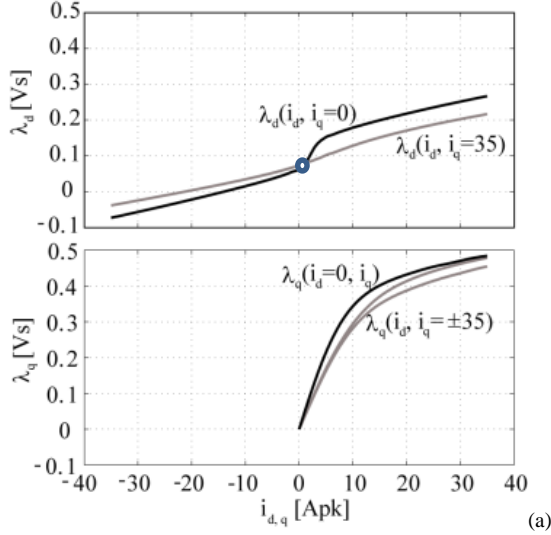


Figure 5. a) dq flux linkage curves of the motor under test (see Table I). The flux LUTs refer to this experimental data. The blue circle indicates the PM flux linkage; b) Contour lines of L_d in the dq current plane, in [mH]; c) contour lines of L_q , in [mH].

C. Current Prediction

The dq voltage equations (24) are integrated in discrete form (25) for prediction of the stator current components at time t_{k+1} :

$$\begin{cases} v_d = R_s i_d - \omega \lambda_q + L_d \frac{di_d}{dt} \\ v_q = R_s i_q + \omega \lambda_d + L_q \frac{di_q}{dt} \end{cases} \quad (24)$$

$$\begin{cases} \hat{i}_d(k+1) = i_d(k) e^{-\frac{R_s T_{sw}}{L_d}} + \frac{v_d(k) + \omega \lambda_q(k)}{R_s} \left(1 - e^{-\frac{R_s T_{sw}}{L_d}}\right) \\ \hat{i}_q(k+1) = i_q(k) e^{-\frac{R_s T_{sw}}{L_q}} + \frac{v_q(k) - \omega \lambda_d(k)}{R_s} \left(1 - e^{-\frac{R_s T_{sw}}{L_q}}\right) \end{cases} \quad (25)$$

It is assumed that the dq inductances do not vary during one sampling period. In Fig. 4 the exponentials in the two equations (25) have been substituted with their first-order approximations.

D. Flux Linkage at Time t_{k+1}

The flux linkages $\hat{\lambda}_d(k+1)$ and $\hat{\lambda}_q(k+1)$ are evaluated from $\hat{i}_d(k+1)$, $\hat{i}_q(k+1)$, $L_d(k)$ and $L_q(k)$ according to (7). Finally, the outputs needed for the control are obtained, as indicated in Fig. 4:

- amplitude of the stator flux linkage vector $\hat{\lambda}(k+1)$;
- flux phase angle, referred both to the $\alpha\beta$ stationary frame $\hat{\theta}_s(k+1)$ and the dq synchronous frame $\hat{\delta}(k+1)$.
- quadrature component of stator current $\hat{i}_{qs}(k+1)$.

V. SIMULATION AND EXPERIMENTS

Experimental tests and simulations were carried out on a PMASR motor drive for validation of the proposed control scheme. Other two control techniques, based on PI closed loop control are also considered, for the sake of comparison.

Table I summarizes the ratings of the drive under test. The PMASR motor is designed for traction and its rotor stack is represented in Figure 6a, showing the multiple-barrier per pole structure. The drive control was first tested in simulation using Matlab/Simulink. Then a dedicated experimental rig was used, equipped with a dSPACE 1103 PPC controller board [16] and an incremental encoder with 512 cycles per revolution. Fig. 6b reports a picture of the experimental setup. The red rectangles put in evidence the motor under test and the power converter. The computer on the table is the dSPACE host computer.

TABLE I. RATINGS OF THE PM-ASSISTED SYNCHRONOUS RELUCTANCE MOTOR DRIVE

| Motor Data | |
|----------------------|-----------------------------------|
| Continuous power | 7 kW |
| Peak power | 10 kW |
| Base Speed | 2200 rpm |
| Maximum speed | 10000 rpm |
| Stator resistance | 0.3 Ohm |
| Rotor inertia | $4.6 \cdot 10^{-3} \text{ kgm}^2$ |
| Inverter Data | |
| Switching frequency | 10 kHz |
| DC voltage | 350 V |
| Maximum current | 33 Apk |
| Modulation Technique | Space Vector Modulation |

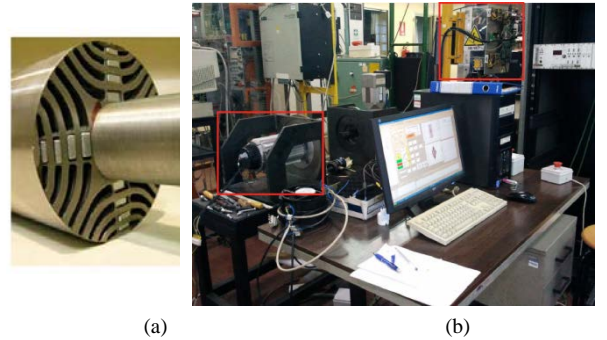


Figure 6. a) Rotor of the motor under test. b) Experimental setup based on the dSPACE 1103 Power PC controller board.

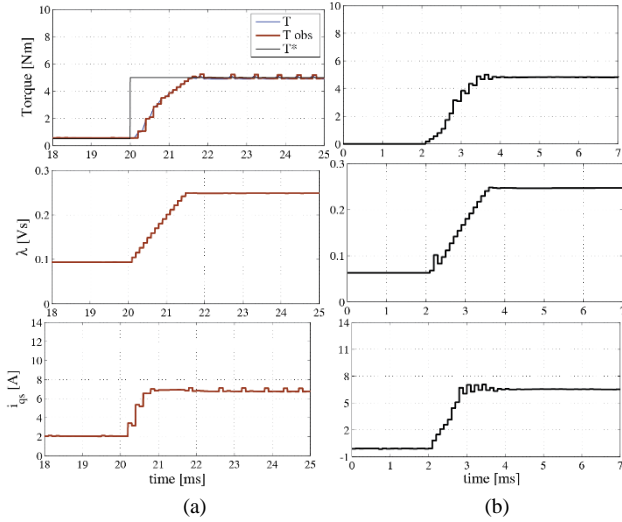


Figure 7. Simulated (a) and experimental (b) response to a 5 Nm torque step starting from zero speed. During the test the speed ramps up to 70 rpm. From top to bottom: estimated torque, observed flux magnitude, quadrature current.

A. Torque Step Response

The torque step and torque reversal responses are reported, to assess the dynamic response of the proposed control. The plots in Fig. 7 compare the experimental and simulated responses to a 5 Nm torque reference step. The shaft of the machine under test is free, no outside load is applied to it, and the speed is zero at the time of the torque reference step and grows after the torque step. Final speed is low (<100 rpm).

B. Comparison with PI-based Controllers

In Fig. 8 the 5 Nm torque step test is repeated against two non-predictive competitors: the PI-based DFVC of [3] and a standard Current Vector Control (CVC). The CVC uses MTPA lookup tables to produce the i_d^*, i_q^* reference values according to the torque reference.

The torque response of the proposed DFVC and the one of the CVC are comparable, whereas the PI-based version of the DFVC has a slower response. Different settings of the PI regulators of this latter controller could produce a better response at the expense of worse behavior in other situations. This to say that the PI-based DFVC would need adaptation of the q_s regulator parameters according to the operating point to reproduce the same response of the predictive DFVC algorithm presented here. Instead, the CVC has a very good dynamic response, but it is less handy than the DFVC when dealing with the flux weakening and the MTPV high-speed region [17].

The response of the predictive DFVC to the 5 Nm reference step, in Figs. 7 and 8, is non dead-beat. No controller could be dead-beat in these circumstances, due to the limited Volt-seconds available in one beat and the significant flux linkage excursion involved in the 5 Nm torque variation. All PM machines with a high per-unit inductance (that is, the ones with flux-weakening capability, salient or not) require substantial Vs variations for torque regulation, independently of the adopted controller.

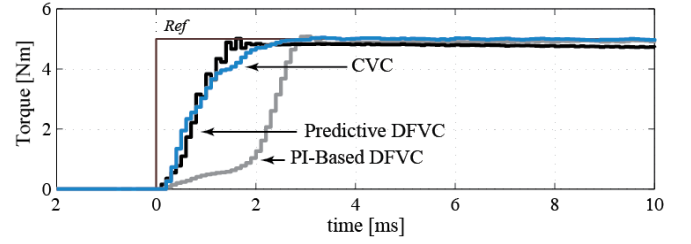


Figure 8. Experimental results for a 5 Nm torque step. For the predictive DFVC the attenuation coefficient k_a is equal to 0.8. Estimated torque waveforms. Free shaft. Initial speed is zero. Final speed is nearly 70 rpm.

C. Torque Reversal

Torque reversals can produce transient overcurrent, unhandled by the maximum current limitation block of Fig. 3. Fig. 9a reports the simulated flux linkage trajectories during a torque reversal transient, for the different control techniques. The torque is reversed between plus and minus 34 Nm, corresponding to the maximum current overload ($I_{max} = 35$ Apk). This issue is specific of very salient machines as the one under analysis.

In Fig. 9a the CVC drives the flux linkage vector safely along a vertical line, with the d -component nearly constant and the q -component spanning between maximum positive and maximum negative for torque transition.

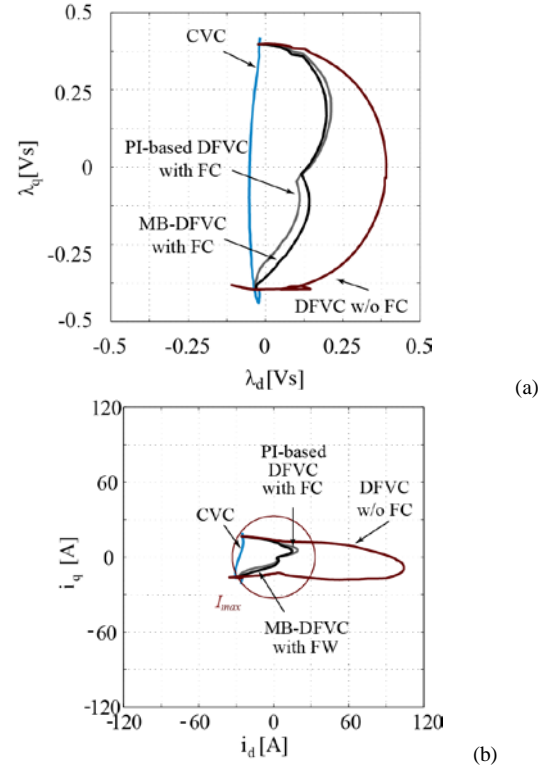


Figure 9. Simulation results: trajectories of the flux linkage (a) and current (b) vectors in the respective dq planes during a maximum torque reversal. Free shaft. Torque reversal occurs when at 1000 rpm.

DFVC, on the contrary, imposes a swift rotation of the flux linkage vector by regulation of the torque angle δ : the flux linkage follows a semi-circular trajectory indicated with “DFVC” in Fig. 9a. Start and end points are the same of the CVC cases, but the magnetic states explored during the excursion are very different. In Fig. 9b the current trajectories corresponding to Fig. 9a are reported, in the i_d, i_q

plane. The flux vector rotation imposed by the DFVC produces the transient overcurrent indicated with “DFVC”, that leads the current vector amplitude up to three times the I_{max}^* current limit, and over, even in presence of the i_{qs}^* saturation block of Fig. 3. Provided the large saliency of the machine, the current peak is reached when the flux linkage vector is aligned with the minimum inductance axis (d -). In other words, being the flux amplitude constant, the current along the minimum inductance axis is magnified. The same tests on a poorly salient machine (single layer IPM motor) did not evidence the problem.

The countermeasure used here is called “Flux Clamping” (FC), and consists in limiting the flux amplitude when the load angle is close to zero. When the observed δ angle is close to zero, then the flux linkage amplitude is set to be equal to the open-circuit flux linkage value. In Fig. 9 the FC is applied to both the DFVC techniques, showing acceptable results. The proposed controller is indicated as MB-DFVC in the figure (MB stands for “Model Based”). The details of the “FC” implementation are not reported, for the sake of brevity. Moreover, this is a side aspect of the algorithm proposed here, limited to the niche of PM-assisted Synchronous Reluctance machines.

D. Phase Current Waveforms

Figure 10 reports the phase duty cycle and phase current waveforms during a deceleration from 1800 rpm to minus 2000 rpm. The currents are fairly sinusoidal. If switching harmonics (not shown in the figure) are neglected, the THD of the phase currents is of a few percent also at very low speed. The duty-cycle waveforms are the ones typical of space vector modulation.

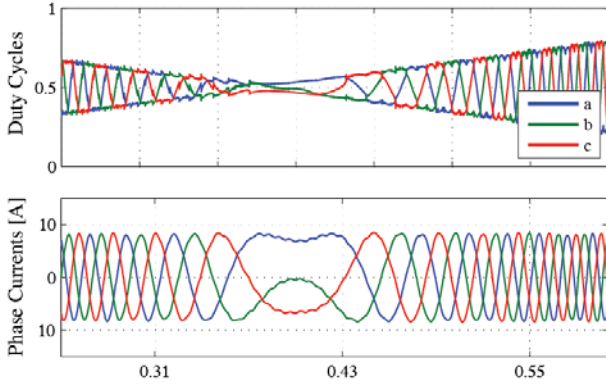


Figure 10. Experimental results: phase duty cycles (top) and phase currents (bottom) during a slow speed reversal at constant torque (5 Nm). Speed varies from 1800 rpm positive to 2000 rpm negative.

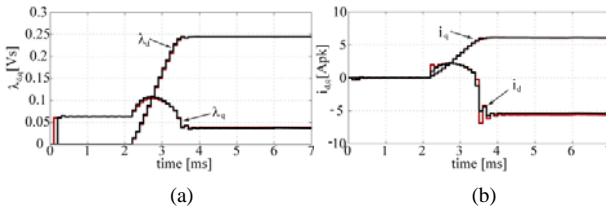


Figure 11. Simulation results, referring to a 5 Nm torque step as the one in Fig. 7a. a) flux linkage predicted at $t(k+1)$ (red), actual flux linkage (black) components; b) predicted stator current (red), actual stator current (black) components.

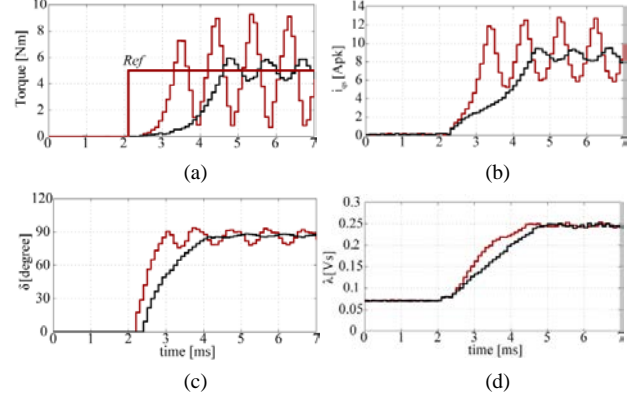


Figure 12. Effect of the actuation delay: experimental response to a 5 Nm torque step, with a non-predictive flux observer. a) Observed torque, b) torque current (i_{qs}), c) observed load torque angle, d) observed flux magnitude. The red curves have $k_a=1$, the black ones have $k_a=0.4$.

E. States Prediction as Key Enabling Technology

Figure 11 compares the flux linkages and currents predicted by the observer with the actual machine states, in simulation. The flux linkage components are identical at all times, transients included, while the d -axis current has small discrepancies at the beginning and at the end of the torque transient.

Moreover, additional experimental tests were carried out to put in evidence the consequences of incorrect implementation of this enabling block. If the values of currents and flux linkages at the present instant t_k are used instead of the t_{k+1} predicted ones, the controlled quadrature current and the torque are affected by an intrinsic oscillatory behavior, as suggested by the plots reported in red in Fig. 12. A ready mitigation of such undesired effect is to apply an attenuation coefficient $k_a (< 1)$ [8,9] to the delta angle error in the q_s voltage equation:

$$v_{qs}^*(k) = R_s \cdot \hat{i}_{qs}(k) + \left(k_a \frac{\Delta \hat{\delta}^*}{T_{sw}} + \omega \right) \cdot \hat{\lambda}(k) \quad (26)$$

A pure model-based controller has $k_a = 1$. Respect to equation (5), the observed flux linkage and the measured i_{qs} at time (k) are used instead of time ($k+1$) extrapolations. The attenuation factor can be used instead of ($k+1$) states prediction, at the expense of a reduced dynamic response. In Fig. 12 the non-predictive case is reported with $k_a = 1.0$ (oscillatory) and $k_a = 0.4$ (slow response), showing that the torque response is slower than the ones obtained in Figs. 7 and 8.

F. Effect of L_d , L_q Adaptation

Simulation tests were carried out to quantify the effects of the adaptive inductances calculation. The plots in Figure 13 summarize the results. The torque reference is varied in four steps from zero to 30 Nm at standstill. The two situations with and without inductance adaptation are compared (Fig. 13a). The waveforms of the instantaneous inductance values are represented in Fig. 13b and 13c. With constant L_d and L_q values (red lines in Figs. 13b and 13c, $L_d = 3$ mH, $L_q = 24$ mH) the torque response is:

- 1) inaccurate in terms of steady state value;
- 2) the dynamic response is sometimes underdamped and sometimes not;

- 3) A higher noise is noticed at all torque levels.

Steady-state error comes from flux estimation error. With wrong inductances, time $(k+1)$ observed flux is wrong both in amplitude and phase, and so will be the delivered torque. The misestimate of the feedback causes the steady state error. Going to the erratic dynamic response, this comes from the combination of the flux vector misestimate, that introduces error in (5) mainly through $\Delta\lambda$ and $\Delta\delta$, with the direct effect of wrong $L_d(k)$, $L_q(k)$ into equation (16). Therefore, the voltage vector is affected by several errors, whose consequences can be less or more severe according to the distance of the adopted L_d , L_q constants from actual values in same operating conditions. Augmented noise is an expected trend, when dealing with model errors in model-based control.

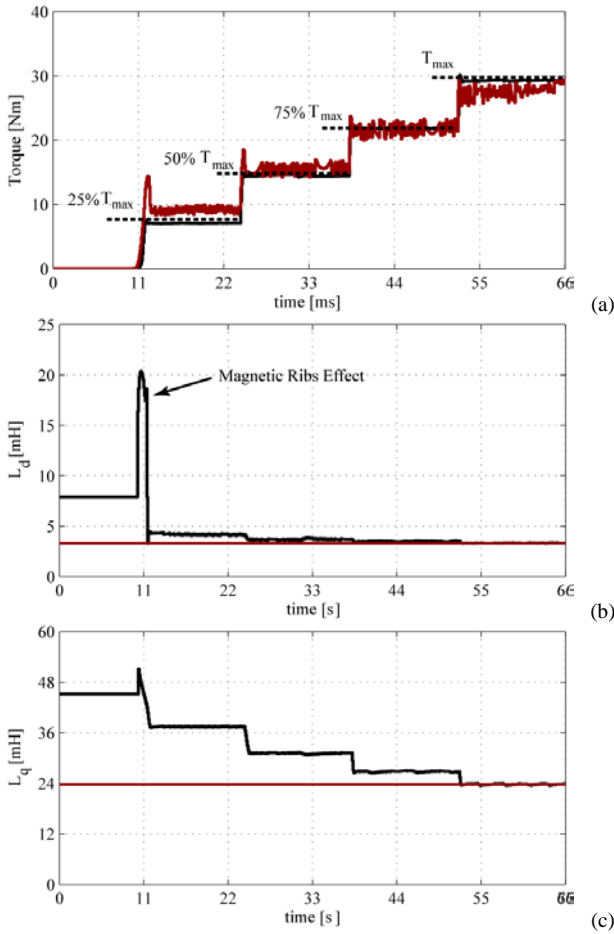


Figure 13. Simulation results: torque response with and without the adaptive calculation of the stator inductances (black and red lines, respectively). a) Torque; b) estimated L_d ; c) estimated L_q . Standstill conditions (locked rotor).

G. Detuning from PM Temperature Variation

The temperature of PMs has the effect of detuning the control parameter λ_m . Such parameter affects $L_d(k)$, $L_q(k)$ evaluation and therefore calculation of $\hat{\lambda}_d(k+1)$, $\hat{\lambda}_q(k+1)$. The PM-assisted machine under test has a low per-unit PM flux linkage: in Fig. 5a the PM flux linkage is evidenced with a circle and is 0.06 Vs, whereas the q -flux linkage can go to 0.4 Vs and beyond. This to say that the effect of PM temperature are hardly visible with this machine. Tests run with different machines are reported in [20], showing that a

misestimate of the control parameter λ_m produces torque misestimate. If the temperature effect is not compensated, a hot machine produces less torque than the reference one. This effect is very similar to what happens with other controllers, such as CVC: a hot machine gives less torque than a cold machine, for the same current. When required by the application, the control can be augmented with one of the techniques for λ_m detuning compensation existing in the literature, such as the one in [21].

H. Flux Weakening Operation

The closed-loop speed control response is documented in Figures 14 and 15. An 8000 rpm speed reference step is applied to account for the current and voltage limited speed operating region, including the MTPV region. Fig. 14 reports the speed and torque responses for the PI- and PA-DFVCs. Expectedly, the waveforms of the two algorithms are superimposed. Fig. 15 reports the controlled variables λ , i_{qs} along with the intermediate control variable δ , the machine phase currents and duty-cycles. The speed region indicated as “current limitation” is the voltage and current limited region [5], whereas the MTPV speed region is the one where the load angle δ is constant and maximum ($\delta_{max} = 124^\circ$). Figs. 14 and 15 confirm the well-known consideration that direct-flux controllers can handle the flux weakening operating region ideal wise and without the heavy modelling manipulation required by the CVC [17], where 2-dimensional tables of the i_d^* , i_q^* references as a function of torque and speed are needed (...).

VI. CONCLUSION

A model-based version of the Direct Flux Vector Control algorithm was presented and successfully tested in simulation and experiments. Closed form equations are used for the calculation of the converter commands, including the original evaluation of the load angle error in explicit form.

The inverter voltage and current limits are exploited in a model-independent manner, as usual for direct flux type controllers. The MTPV limit is handily exploited thanks to the mentioned explicit expression of the load angle error.

The observer presented in the paper is the key element of this implementation. The machine parameters are segregated in a single block, included in the observer, in the non-manipulated form of flux linkage look-up tables, directly coming from experimental identification. The dq inductances are on-line evaluated in real-time and this improves the control precision and avoids chattering.

The comparison with PI-based DFVC and current vector control confirms that the proposed controller retains the advantageous properties of direct flux and torque controllers, with ease of flux weakening and good torque dynamics. With respect to current vector control, the presented algorithm reduces the model manipulation burden, at the expense of a more complicate flux observer scheme.

Torque reversal conditions were investigated to put in evidence the risk of overcurrent, when flux linkage amplitude is imposed to a machine with high saliency. A countermeasure called “Flux Clamping” has been proposed and tested.

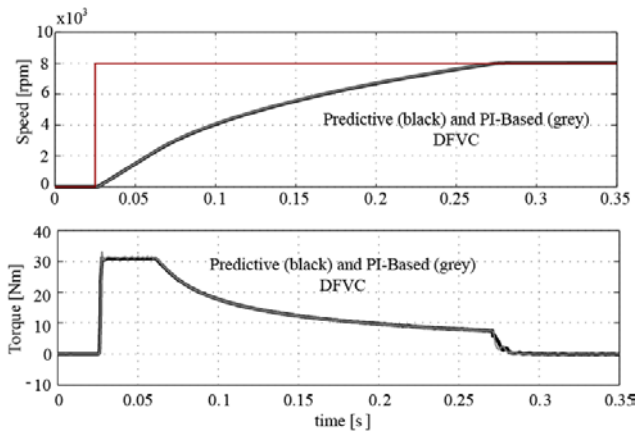


Figure 14. Simulated response to a 8000 rpm speed reference step.

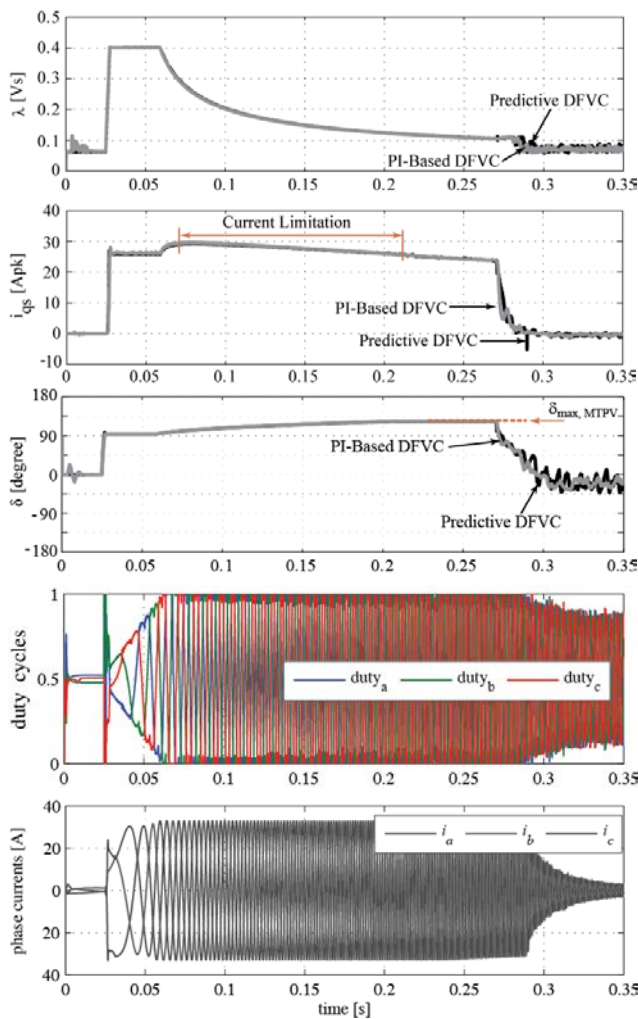


Figure 15. Simulation results: controlled variables of the two versions of the DFVC, during the speed transient of Figure 13. a) stator flux linkage amplitude; b) q_s current; c) load torque angle; d) phase duty-cycles e) phase currents.

REFERENCES

- [1] Buja, G.S.; Kazmierkowski, M.P.; , "Direct torque control of PWM inverter-fed AC motors - a survey," *Industrial Electronics, IEEE Transactions on* , vol.51, no.4, pp. 744- 757, Aug. 2004
- [2] Inoue, Y.; Morimoto, S.; Sanada, M.; , "Control Method Suitable for Direct-Torque-Control-Based Motor Drive System Satisfying

- Voltage and Current Limitations," *Industry Applications, IEEE Transactions on* , vol.48, no.3, pp.970-976, May-June 2012
- [3] Pellegrino, G.; Bojoi, R.I.; Guglielmi, P.; , "Unified Direct-Flux Vector Control for AC Motor Drives," *Industry Applications, IEEE Transactions on* , vol.47, no.5, pp.2093-2102, Sept.-Oct. 2011
- [4] Kukrer, O.; , "Discrete-time current control of voltage-fed three-phase PWM inverters," *Power Electronics, IEEE Transactions on* , vol.11, no.2, pp.260-269, Mar 1996
- [5] Morimoto, S.; Sanada, M.; Takeda, Y.; , "Wide-speed operation of interior permanent magnet synchronous motors with high-performance current regulator," *Industry Applications, IEEE Transactions on* , vol.30, no.4, pp.920,926, Jul/Aug 1994
- [6] Jae Suk Lee; Chan-Hee Choi; Jul-Ki Seok; Lorenz, R.D.; , "Deadbeat-Direct Torque and Flux Control of Interior Permanent Magnet Synchronous Machines With Discrete Time Stator Current and Stator Flux Linkage Observer," *Industry Applications, IEEE Transactions on* , vol.47, no.4, pp.1749-1758, July-Aug. 2011
- [7] Preindl, M.; Bolognani, S.; , "Model Predictive Direct Speed Control with Finite Control Set of PMSM Drive Systems," *Power Electronics, IEEE Transactions on* , vol.28, no.2, pp.1007,1015, Feb. 2013
- [8] Maes, J.; Melkebeek, J.; , "Discrete time direct torque control of induction motors using back-EMF measurement," *Industry Applications Conference, 1998. Thirty-Third IAS Annual Meeting. The 1998 IEEE* , vol.1, no., pp.407-414 vol.1, 12-15 Oct. 1998
- [9] Kenny, B.H.; Lorenz, R.D.; , "Stator- and rotor-flux-based deadbeat direct torque control of induction machines," *Industry Applications, IEEE Transactions on* , vol.39, no.4, pp. 1093- 1101, July-Aug. 2003
- [10] N. Bianchi and S. Bolognani, "Magnetic models of saturated interior permanent magnet motors based on finite element analysis," in *IEEE Industry Applications Conference IAS 1998*, vol. 1, Oct. 1998, pp. 27-34 vol.1.
- [11] Morimoto, S.; Takeda, Y.; Hirasa, T.; Taniguchi, K.; , "Expansion of operating limits for permanent magnet motor by current vector control considering inverter capacity," *Industry Applications, IEEE Transactions on* , vol.26, no.5, pp.866,871, Sep/Oct 1990
- [12] Pellegrino, G.; Armando, E.; Guglielmi, P.; , "Direct-Flux Vector Control of IPM Motor Drives in the Maximum Torque Per Voltage Speed Range," *Industrial Electronics, IEEE Transactions on* , vol.59, no.10, pp.3780,3788, Oct. 2012
- [13] P. L. Jensen and R. D. Lorenz "A physically insightful approach to the design and accuracy assessment of flux observers for field oriented induction machine drives", *IEEE Trans. Ind. Appl.*, vol. 30, no. 1, pp.101 -110 1994.
- [14] Armando, E.; Bojoi, R.I.; Guglielmi, P.; Pellegrino, G.; Pastorelli, M.; , "Experimental Identification of the Magnetic Model of Synchronous Machines," *Industry Applications, IEEE Transactions on* , vol.49, no.5, pp.2116,2125, Sept.-Oct. 2013.
- [15] K. Rahman and S. Hiti "Identification of machine parameters of a synchronous motor", *IEEE Trans. Ind. Appl.* , vol. 41, no. 2, pp. 557 -565 2005.
- [16] <http://www.dspace.com/>
- [17] Tae-Suk Kwon; Gi-Young Choi; Mu-Shin Kwak; Seung-Ki Sul; , "Novel Flux-Weakening Control of an IPMSM for Quasi-Six-Step Operation," *Industry Applications, IEEE Transactions on* , vol.44, no.6, pp.1722,1731, Nov.-dec. 2008
- [18] Bolognani, S.; Calligaro, S.; Petrella, R.; , "Adaptive Flux-Weakening Controller for Interior Permanent Magnet Synchronous Motor Drives," *Emerging and Selected Topics in Power Electronics, IEEE Journal of* , vol.2, no.2, pp.236,248, June 2014
- [19] Pellegrino, G.; Boazzo, B.; Jahns, T.M.; , "Magnetic Model Self-Identification for PM Synchronous Machine Drives," *Industry Applications, IEEE Transactions on* , vol.99, pp.1,1
- [20] Pellegrino, G.; Boazzo, B.; Jahns, T.M.; , "Direct Flux Control of PM synchronous motor drives for traction applications," *Transportation Electrification Conference and Expo (ITEC), 2014 IEEE*, pp.1,6, 15-18 June 2014
- [21] Krishnan, R.; Vijayaraghavan, P.; , "Fast estimation and compensation of rotor flux linkage in permanent magnet synchronous machines," *Industrial Electronics, 1999. ISIE '99. Proceedings of the IEEE International Symposium on* , vol.2, no., pp.661,666 vol.2, 1999
- [22] Lascu, C.; Boldea, I.; Blaabjerg, F.; , "Super-twisting sliding mode control of torque and flux in permanent magnet synchronous machine drives," *Industrial Electronics Society, IECON 2013 - 39th Annual Conference of the IEEE* , vol., no., pp.3171,3176, 10-13 Nov. 2013